Modified Cam-Clay Model for Large Stress Ranges and its Predictions for Geological and Drilling Processes

Mahdi Heidari[1], Maria A. Nikolinakou[1], Peter B. Flemings[2]

[1]Bureau of Economic Geology, The University of Texas at Austin, 10100 Burnet Road, Building PRC-130, Austin, TX 78758, USA

[2]Department of Geological Sciences and Institute for Geophysics, Jackson School of Geosciences, The University of Texas at Austin

Corresponding author: Mahdi Heidari (mahdiheidari@utexas.edu)

Key points:

- The Modified Cam-Clay model is modified to include the stress dependency of the friction angle and the slope of the compression curve.
- The new model predicts the stress-dependency of the mudrock behavior including the K_0 stress and the undrained strength ratios.
- The stress dependency of the friction angle significantly impacts topography of critical wedges and stability of wellbores and channels.

Keywords: Friction angle; Compression curve; Critical-taper theory; Modified Cam-Clay model; Slope stability; Drilling window; in situ stresses

Abstract

We modify the Modified Cam-Clay (MCC) model for large stress ranges encountered in geological applications. The MCC model assumes that the friction angle and the slope of the compression curve of a mudrock are constant and thus predicts constant values for the lateral effective stress ratio under uniaxial strain (K_0) and the undrained strength ratio ($\frac{S_u}{\sigma'_{v0}}$). Experimental work, however, show that these properties vary significantly with stress over large stress ranges (up to 100 MPa). We incorporate the stress dependency of the friction angle and the slope of the compression curve into the MCC model. The modified model, with only one additional parameter, successfully predicts the stress dependency of the stress (K_0) and strength ($\frac{S_u}{\sigma'_{v0}}$) ratios. We encode the modified model and use it in the finite-element analysis of a salt basin in the deepwater Gulf of Mexico. The new model predicts that the stress field around salt is significantly different than predicted by the original MCC model. We also illustrate that the stress dependency of the friction angle has significant consequences for drilling and geological processes: it causes 1) a concave profile for the topography and convex profile for thrust faults in critical wedges with planar décollement; 2) higher magnitudes and narrower range for appropriate mud weights for drilling a wellbore; and 3) deep-seated failure of submarine channel levees at a lower angle. Our study could improve in situ stress and pore pressure estimation, wellbore drilling, and quantitative understanding of geological processes.

Table 1: Nomenclature

Symbol	Description
ρ	Bulk density of sediments
ρ_w	Density of pore water
g	Gravitational acceleration
α_w	Dipping of the surface of a critical wedge
β_w	Dipping of décollement
μ_b	Sliding friction coefficient of décollement
ϕ_b	Friction angle of décollement
ϕ	Internal friction angle
ϕ_{mb}	Internal friction angle at the wedge-base stress level
H	Thickness of a critical wedge
X	Horizontal distance along a critical wedge
σ_1'	Effective maximum principal stress
σ_2'	Effective intermediate principal stress
σ_3'	Effective least principal stress
σ_m'	Effective mean stress
σ_v'	Effective vertical stress
σ_{v0}'	Pre-consolidation vertical effective stress
σ_v	Total vertical stress
σ_1	Total maximum principal stress
σ_3	Total least principal stress
h	Height of slope
α	Central angle of failure surface in a slope
β	Slope angle
ρ'	Bulk density of sediments less density of sea water
ρ_{ws}	Density of sea water
u	Pore pressure
u_h	Hydrostatic pressure
λ^*	Overpressure ratio

K_0	Ratio of effective horizontal to vertical stress under uniaxial strain
S_u	Undrained strength
$\frac{S_u}{\sigma'_{v0}}$	Undrained strength ratio
$\boldsymbol{\varepsilon}$	Total strain tensor
$\boldsymbol{\varepsilon^e}$	Elastic strain tensor
$\boldsymbol{\varepsilon^p}$	Plastic strain tensor
$\boldsymbol{\sigma'}$	Effective stress tensor
e	Void ratio
κ	Slope of recompression line
q	Deviatoric (shear) stress
M	Slope of failure envelope
σ'_{m_0}	Isotropic pre-consolidation stress
$f(\boldsymbol{\sigma'})$	Yield function
Λ	Multiplier of plastic strain increment tensor
N	Intercept of isotropic normal compression line
λ	Slope of isotropic normal compression line
$\sigma'_{m_{cr}}$	Mean effective stress at critical (failure) state
M_0	Coefficient of power-law failure envelope
m	Power of power-law failure envelope
λ_0	Coefficient of power-law isotropic normal compression curve
n	Power of power-law isotropic normal compression curve
κ_0	Coefficient of power-law recompression curve
$P_{collapse}$	Minimum mud pressure for limited wellbore breakout
W	Weight of failing mass in a slope
l	Leverage of weight of failing mass in a slope
R	Radius of failure surface in a slope
γ	Dipping of failure surface in a slope
z	Depth from slope top surface

κ_{salt}	Slope of isotropic compression line of rock salt

1 Introduction

The friction angle and the compression curve are two of the most critical rock parameters for many geological and hydrocarbon-production processes. Friction angle controls the geometry and activity of faults (Hubbert and Rubey, 1959; Suppe, 2007), the stability of earth slopes (Hubbert and Rubey, 1959; Sawyer et al., 2014; Stigall and Dugan, 2010), and the geometry of critical tapers such as in accretionary wedges and fold-and-thrust belts (Dahlen, 1990; Davis et al., 1983; Gao et al., 2018). Friction angle also impacts hydrocarbon production in different ways. It affects the ratio of horizontal to vertical effective stress under uniaxial strain (K_0) and thereby the least principal stress, which is a key control on the maximum hydrocarbon column in reservoirs (Flemings et al., 2002) and appropriate mud pressures for drilling wellbores (Alberty and McLean, 2004). The compression curve is a central factor in basin subsidence and deposition, pore pressure prediction (Hart et al., 1995), and seismic models and interpretation (Cook and Sawyer, 2015).

The friction angle and the slope of the compression curve are typically assumed to be constant for a rock in the analyses of geologic processes. Examples include analytical models such as the critical-taper theory (Dahlen, 1990; Davis et al., 1983), the limit-state slope stability models (Hubbert and Rubey, 1959; Sawyer et al., 2014; Stigall and Dugan, 2010), the Earth's strength profiles (Suppe, 2014), and wellbore stability models (Zoback, 2010). The assumption of constant rock properties is typical in numerical analyses too. For example, the Modified Cam-Clay (MCC) model, a commonly-used constitutive model in finite-element analyses, assumes that the friction angle and the slope of the compression curve are constant and thus predicts

constant values for the K_0 stress ratio and the undrained strength ratio ($\frac{S_u}{\sigma'_{v0}}$). The assumption of constant rock properties is based on experimental observations over small stress ranges typically encountered in geotechnical engineering practice (< 1 MPa) (Muir Wood, 1990).

Experimental tests carried out on mudrocks over large stress ranges encountered in geological settings (~ 100 MPa), however, show that the friction angle and the slope of compression curve are not constant but both vary substantially with stress. For example, Bishop et al. (1965) conducted undrained shear tests on London Clay samples that were resedimented and consolidated under isotropic stress of up to 7.5 MPa. They reported that as stress increased from low values to 6 MPa, the undrained strength ratio decreased from 0.24 to 0.2, and friction angle decreased from 21^o to 16.1^o. Yassir (1989) conducted undrained shear tests on soils from a mud volcano in Taiwan that were resedimented and uniaxially consolidated. They reported a decrease in the friction angle from 26.1^o to 22.6^o when stress increased from 5 MPa to 68 MPa. Saffer and Marone (2003) made similar observations on the friction angle of illite- and smectite-rich shales; they used a biaxial shear device to measure the friction angle for a large normal stress range of 5 to 150 MPa and observed that as the normal stress increased over this range, the coefficient of friction decreased from 0.30 to 0.07 for the smectitic shales and from 0.63 to 0.41 for the illitic shales. Similarly, Ikari et al. (2007) conducted biaxial shear tests at different normal stresses of up to 100 MPa on Na- and Ca-montmorillonite-based fault gouges with different water and quartz contents and observed that the coefficient of friction in all cases decreased significantly with increase in normal stress (see Moore and Lockner (2007) for more references). Jones (2010) conducted undrained shear tests on resedimented Ugnu Clay from Northern Alaska for stresses of up to 10 MPa and reported that the friction angle decreased from 35.1^o to 23.6^o when stress increased from 0.2 MPa to 9.8 MPa; they also observed a decrease in the undrained

strength ratio and an increase in the K_0 ratio with stress. Recently, Abdulhadi et al. (2012) and Casey et al. (2016) conducted a series of triaxial and uniaxial tests on resedimented mudrocks with a wide variety of lithology and composition for a stress range of 0.1-100 MPa and observed that the residual (post-peak) friction angle, the K_0 ratio, and the undrained strength ratio of all mudrocks varied systematically with stress. For instance, for resedimented material from a highly plastic (liquid limit=79%; clay fraction=63%), smectite-rich (smectite=87% of clay fraction) mudrock in the Eugene Island 330 field, Gulf of Mexico, (hereafter termed RGoM EI), as stress increased from 0.3 MPa to 63 MPa, the friction angle decreased dramatically from nearly 32 degrees to 12 degrees, the K_0 stress ratio increased from 0.55 to 0.91, and the undrained strength ratio decreased from 0.3 to 0.1 (Table 2; points, Fig. 1b-d). Experimental data also show that the compression behavior of mudrocks and sands does not follow a linear trend over large stress ranges (Mesri and Olson, 1971; Pestana and Whittle, 1995; Velde, 1996). This behavior was also reported in tests conducted by Casey et al. (2019) (points, Fig. 1a).

In this paper, we modify the Modified Cam-Clay (MCC) constitutive model to incorporate the stress dependency of the friction angle and the slope of the compression curve. The MCC model is the most widely used constitutive model to describe the behavior of clays and poorly lithified mudrocks because, with a minimal number of parameters, it satisfactorily represents essential mechanical characteristics of mudrocks such as dependence on the confining stress, strain hardening and softening, and the critical state (Muir Wood, 1990; Roscoe and Burland, 1968). We calibrate the new model with the friction angles and the nonlinear compression curve measured over a stress range of 0.1-100 MPa for RGoM EI mudrocks (Casey et al., 2016) and use the calibrated model to predict the K_0 ratio, undrained strength ratio, and undrained effective stress paths over a stress range of 0.1-100 MPa. We encode the new MCC model to use it in

conjunction with finite-element code Abaqus to predict stresses in a salt basin in the deepwater Gulf of Mexico. We also incorporate the stress dependency of the friction angle into analytical models developed for the topography of critical wedges, strength profile of Earth's crust, stability of submarine channels, and appropriate drilling window and illustrate the significance of this dependency to these processes.

Table 2: Stresses measurements from triaxial tests on resedimented mudrock samples from Eugene Island, Gulf of Mexico, reported at the end of uniaxial compression and undrained shearing phases (Casey et al., 2016). Rows represent tests at different pre-consolidation stresses (σ'_{v0}).

Uniaxial compression			Undrained shearing			
σ'_{v0}	σ'_{h0}	$K_0 = \frac{\sigma'_{h0}}{\sigma'_{v0}}$	σ'_{vcr}	σ'_{hcr}	$\varphi = sin^{-1}(\frac{\sigma'_{vcr} - \sigma'_{hcr}}{\sigma'_{vcr} + \sigma'_{hcr}})$	$\frac{c_u}{\sigma'_{v0}} = \frac{\sigma'_{vcr} - \sigma'_{hcr}}{2\ \sigma'_{v0}}$
0.356	0.195	0.548	0.314	0.098	31.688	0.304
0.379	0.223	0.589	0.280	0.118	24.134	0.214
0.878	0.583	0.664	0.684	0.304	22.594	0.216
1.959	1.361	0.694	1.649	0.807	20.052	0.215
9.759	7.809	0.800	6.996	4.339	13.556	0.136
63.470	57.789	0.910	38.285	25.219	11.873	0.103

(a) (b)

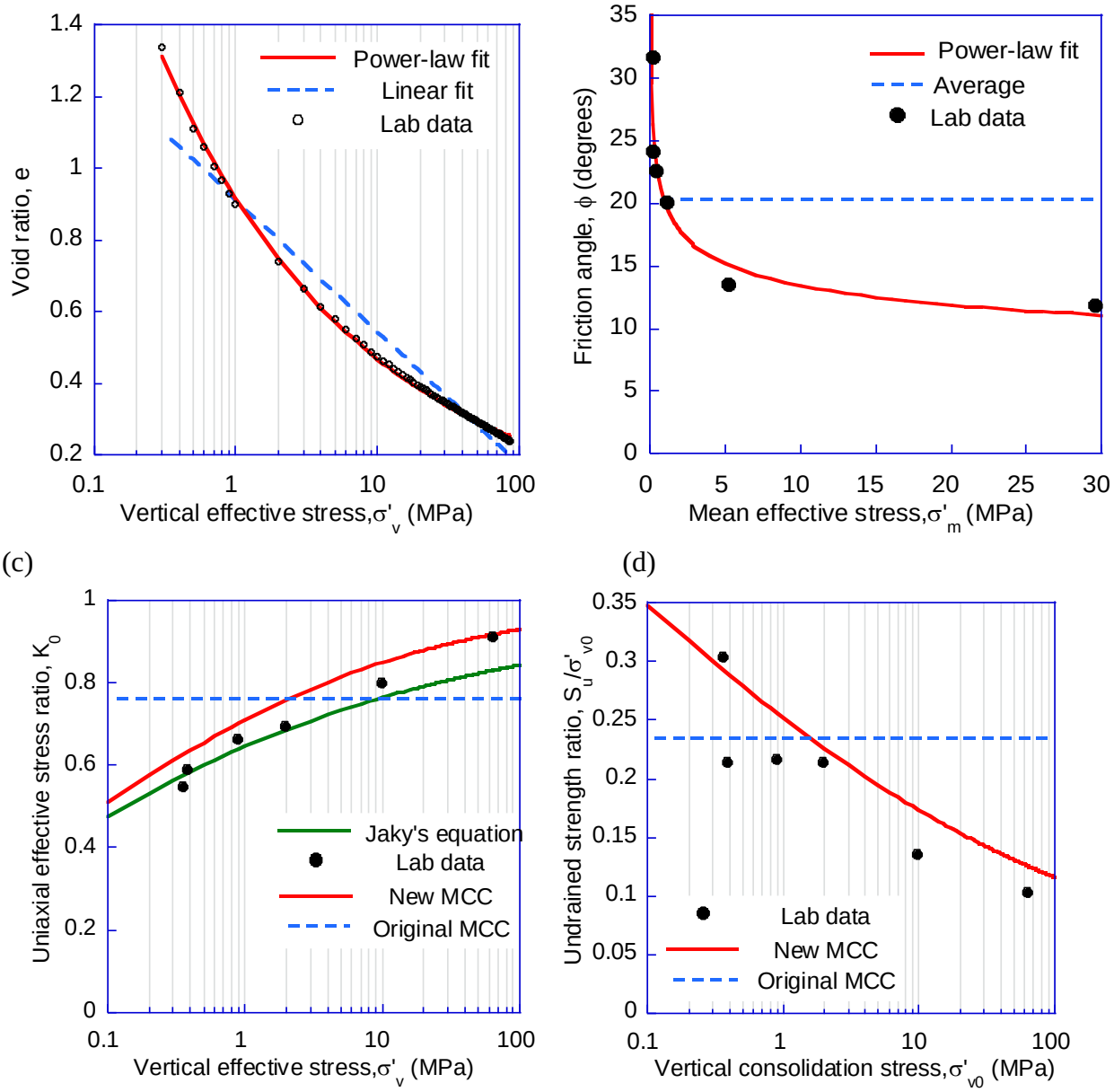

Figure 1: Measured, fitted, and predicted data for RGoM EI mudrocks over a stress range of 0.1-100 MPa. Measured data (dots) are from Casey et al. (2016). (a) Uniaxial compression. Measured data are from CRS consolidation tests. These data follow a nonlinear trend. (b) Friction angle. Measured data represent friction angles at the critical state in undrained triaxial tests. These data show that the friction angle decreases substantially with stress. (c) Uniaxial effective stress ratio (K_0). Measured data are from triaxial tests under uniaxial-strain conditions. These data show that the stress ratio increases substantially with stress. (d) Undrained strength ratio ($\frac{S_u}{\sigma'_{v0}}$). Measured data represent strengths measured at the critical state in undrained triaxial tests on samples uniaxially consolidated to different pre-consolidation stresses (σ'_{v0}). These data show that the undrained strength ratio decreases substantially with stress.

2 A stress-level-dependent MCC model

2.1 MCC model

The MCC model is an elastic-plastic model; the total strain tensor ($\boldsymbol{\varepsilon}$) is decomposed into elastic ($\boldsymbol{\varepsilon^e}$) and plastic ($\boldsymbol{\varepsilon^p}$) parts:

$$\boldsymbol{\varepsilon} = \boldsymbol{\varepsilon^e} + \boldsymbol{\varepsilon^p}. \quad (1)$$

The elastic strain is obtained from the effective stress tensor $\boldsymbol{\sigma'}$ using Hooke's law. The bulk modulus in this law is obtained from the assumption that void ratio (e) changes linearly with the logarithm of the mean stress ($\sigma'_m = \frac{\sigma'_1+\sigma'_2+\sigma'_3}{3}$) during elastic deformation:

$$de = \kappa \cdot d(\ln(\sigma'_m)), \quad (2)$$

where κ is a constant. The shear modulus is either defined as an independent constant or obtained from the bulk modulus and a constant Poisson's ratio using the relationship between these parameters.

Inelastic (plastic) deformation occurs when stresses increase beyond a limit, which is characterized by the yield surface in the stress plot. This surface in the MCC model is assumed to have an elliptical form in the $q - \sigma'_m$ stress plot (dashed lines, Fig. 2), where q is the deviatoric stress ($q = \sqrt{\frac{(\sigma'_1-\sigma'_2)^2+(\sigma'_1-\sigma'_3)^2+(\sigma'_2-\sigma'_3)^2}{2}}$):

$$f(\boldsymbol{\sigma'}) = q^2 - M^2 \cdot \sigma'_m \cdot \left(\sigma'_{m_0} - \sigma'_m\right) = 0, \quad (3)$$

In the MCC model, the yield surface is also used to determine plastic strains; the plastic-strain-increment tensor is assumed to be normal to the yield surface (an associated flow rule):

$$d\boldsymbol{\varepsilon^p} = \Lambda \frac{\partial f(\boldsymbol{\sigma'})}{\partial \boldsymbol{\sigma'}} \quad (4)$$

where variable $\Lambda \geq 0$ is a scalar function of stresses.

The MCC model follows the critical-state theory, which states that the volumetric plastic strain increment is zero at the critical (post-peak failure) state. Thus, the crest of the yield surface (points, Fig. 2), at which volumetric plastic strain increment vanishes (Eqn. 4), represents the critical state (Atkinson and Bransby, 1977). Further, parameter M in Eqn. 3, which expresses the slope of the line emanating from the origin to the crest of the yield surface, represents the secant slope of the critical-state (failure) envelope in the $q - \sigma'_m$ stress plot (solid lines, Fig. 2). This parameter can be obtained from the residual (post-peak) friction angle (ϕ) of the rock as $M = \frac{6\sin(\phi)}{3-\sin(\phi)}$.

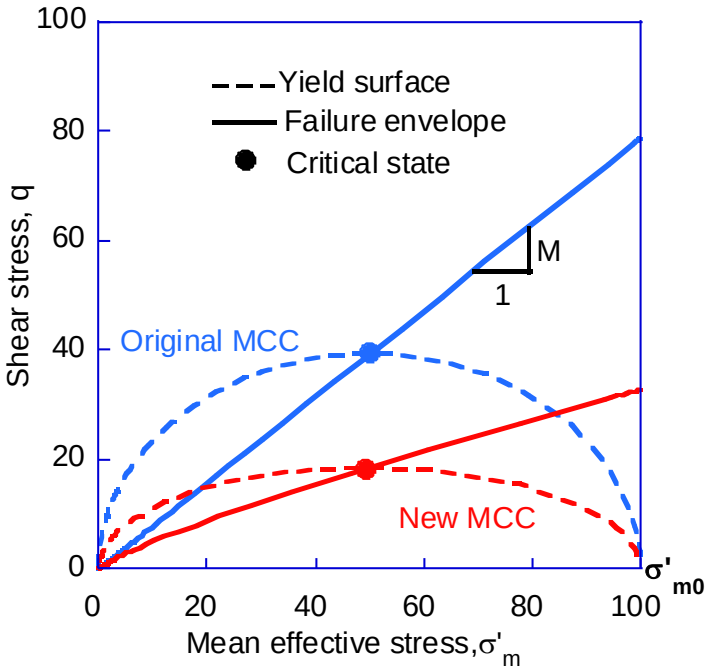

Figure 2: Yield surface and critical-state (failure) envelope in original (blue) and new (red) MCC models. In both models, the yield surface is an ellipsoid and the critical-state envelope passes through the crest of the yield surface. The failure envelope, however, is different in the two models; it is linear in original model and curvilinear in new model.

Variable σ'_{m_0} in Eqn. 3 is the horizontal intercept of the yield surface in the $q - \sigma'_m$ stress plot (Fig. 2) and represents the isotropic pre-consolidation stress. This stress controls the size of the yield surface and is assumed to vary with the volumetric plastic strain. This variation can be obtained from the isotropic normal compression curve, which describes the change in the void ratio during isotropic loading of the rock. In the MCC model, this curve is assumed to be linear when the void ratio is plotted against the logarithm of the mean stress:

$$e = N - \lambda \cdot \ln\left(\sigma'_{m_0}\right) \quad (5)$$

where λ is the slope and N is the intercept of the isotropic normal compression curve at $\sigma'_{m_0} = 1$.

2.2 Modification of MCC model for large stress range

We modify the failure envelope and the normal compression curve in the MCC model to incorporate the stress dependency of the friction angle and the slope of the normal compression curve (Fig. 1a, b).

2.2.1 Nonlinear failure envelope

We replace the linear form of the failure envelope with a power-law form to represent the stress dependency of the friction angle (Fig. 1b). This form of the failure envelope was envisaged in Mohr's pioneering work on failure envelopes (Holtz and Kovacs, 1981). We do this replacement by expressing parameter M, which is the secant slope of the failure envelope, as a power-law function of the mean stress at critical (failure) state ($\sigma'_{m_{cr}}$) as

$$M = M_0 \cdot {\sigma'_{m_{cr}}}^{m}; \quad (6)$$

where $M_0 > 0$ and $m < 0$ are material constants.

199 2.2.2 Nonlinear compression curve

200 We replace the linear form of the normal compression curve with a power-law form to
201 represent the stress dependency of the slope of the compression curve (Fig. 1a):

202 $$e = \lambda_0 \cdot {\sigma'_{m_0}}^{n}; \quad (7)$$

203 where $\lambda_0 > 0$ and $n < 0$ are material constants.

204 The power-law form in Equation 7 leads to a linear relationship between $\ln(e)$ and $\ln(\sigma'_{m_0})$.
205 Pestana and Whittle (1995) studied uniaxial compression of sands with various mineralogy and
206 showed that this linear relationship holds true for sands over large stress ranges. In contrast,
207 Hashiguchi (1974) and Butterfield (1979) proposed a linear relationship between $\ln(1+e)$ and
208 $\ln(\sigma'_{m_0})$. Both the traditional linear relationship (Eqn. 5) and the one that these authors propose
209 have a physically unacceptable property that predict negative porosity at high stresses. Our
210 power-law relationship (Eqn. 7) does not have this issue, predicting zero void ratio at high
211 stresses.

212 In accordance with the normal compression curve, we also replace the linear form of the
213 elastic (unloading-reloading) compression curve with a power-law form with the same power
214 coefficient as the normal compression curve (n, Eqn. 7):

$$de = \kappa_0 \cdot d\left({\sigma'_m}^{n}\right); \quad (8)$$

215 where κ_0 is a constant. Experimental data indicate that the slope of the elastic compression curve
216 decreases with stress and thus the linear form of the elastic compression curve, which assumes a
217 constant slope (κ, Eqn. 2), is not suitable, overestimating the swelling of rocks unloaded at high
218 stresses (Hashiguchi, 1995). Because the slope of the elastic compression curve in our power-law
219 form (Eqn. 8) decreases with stress, our proposed form does not have this experimentally
220 unacceptable property.

In the new MCC model, we modify only the failure envelope (Eqn. 6) and the compression curves (Eqns. 7 and 8). Other components of the MCC model, including the elliptic shape of the yield surface (Eqn. 3) and the associativity of the flow rule (Eqn. 4), are maintained in the new MCC model. In Appendix A, we demonstrate that our enhancements maintain the compatibility of the MCC model with thermomechanical principles.

2.3 Performance of stress-level-dependent MCC model

We first calibrate the original and the new MCC models with the same compression behavior and friction angle data for RGoM EI mudrocks over the stress range of 0.1-100 MPa (Casey et al., 2016). The compression data are available for uniaxial compression (points, Fig. 1a). There is an analytical relation between the parameters of the isotropic and of the uniaxial compression curves in the original MCC model. This relation is used to calibrate the parameters of the isotropic-compression curve in the original MCC model (λ and N, Eqn. 5) from the uniaxial compression data. In the new MCC model, however, because such a relation does not exist, we use trial and error to calibrate the parameters of the isotropic-compression curve (λ_0 and n, Eqn. 7) from the uniaxial compression data. The power-law form proposed in the new MCC model represents the compression data points much more accurately than the linear form in the original MCC model (Fig. 1a).

The parameters of the failure envelope (M_0 and m, Eqn. 6) are determined by plotting values of parameter M for friction angles measured in the compressional triaxial lab tests against the effective mean stresses at failure in these tests ($\sigma'_{m_{cr}} = \frac{\sigma'_{vcr}+2\sigma'_{hcr}}{3}$, Table 2) and fitting a power-law form to the data points. The friction angles obtained from the calibrated failure envelope remarkably fit the measured friction angles (Fig. 1b). An average, constant value of friction

angle, assumed in the original MCC model (dashed line, Fig. 1b), obviously fails to represent the significant variation of the friction angle with stress. Tables 3 and 4 list the value of the material parameters in the original and the new MCC models. The calibrated models are used to predict the K_0 ratio, the undrained strength ratio, and the undrained effective stress paths at different stress levels.

Table 3: Value of input parameters in original MCC model

Parameter	Value
Slope of failure envelope (M)	0.788
Poisson's ratio (ν)	0.1
Intercept of isotropic normal compression line (N)	0.899
Slope of isotropic normal compression line (λ)	0.161
Slope of recompression line (κ)	0.064

Table 4: Value of input parameters in new MCC model

Parameter	Value
Coefficient for slope of failure envelope (M_0)	0.773
Power coefficient for slope of failure envelope (m)	-0.186
Poisson's ratio (ν)	0.1
Coefficient for isotropic normal compression curve (λ_0)	0.882
Power coefficient for isotropic normal compression curve (n)	-0.284
Coefficient for recompression curve (κ_0)	0.35

2.3.1 K_0 and $\frac{S_u}{\sigma'_{v0}}$ ratios

The K_0 and $\frac{S_u}{\sigma'_{v0}}$ ratios that the new MCC model predicts over the large stress range of 0.1-100 MPa vary substantially with stress (red solid lines, Fig. 1c, d). The predicted values of both ratios are in satisfactory agreement with the experimental values (points, Fig. 1c, d), slightly overestimating experimental values at all stress levels. This systematic overestimation is an attribute inherited from the original MCC model. McDowell and Hau (2003) showed that the MCC model has this deficiency because it uses an associated flow rule (Eqn. 4), which leads to overestimation of plastic strains. They showed that this issue can be eliminated if the MCC model is used with a non-associated flow rule. The ratios that the original MCC model predicts are constant (dashed lines, Figs. 1c, d), obviously failing to represent the substantial stress dependency of the ratios. To evaluate the share that the nonlinearity of the failure envelope and the compression curve each has in the stress dependency of the ratios, we predict K_0 and $\frac{S_u}{\sigma'_{v0}}$ ratios for a constant friction angle and a nonlinear compression curve: identical constant values are obtained for both ratios, illustrating that the nonlinearity of the compression curve contributes neither to the magnitude nor to the stress dependency of these ratios.

Several empirical relationships have been suggested between the K_0 ratio of a mudrock and the mudrock friction angle (e.g., Brooker and Ireland, 1965; Mesri and Hayat, 1993). Among them, $K_0 = 1 - \sin(\phi)$ is most widely used (Jaky, 1948; Mayne and Kulhawy, 1982). We use this relation to calculate the K_0 ratio over the effective vertical stress range of 0.1-100 MPa. To obtain the friction angle for a given effective vertical stress, we calculate the effective mean stress at that stress (using the K_0 ratio predicted by the new MCC model (red solid line, Fig. 1c)) and input the calculated mean stress in the friction angle-effective mean stress relation (solid line, Fig. 1b). The K_0 ratios that relation $K_0 = 1 - \sin(\phi)$ produces (green line, Fig. 1c) vary

with stress and satisfactorily predict the measured K_0 ratios at low stresses but underestimate this ratio at high stresses.

2.3.2 Undrained effective stress paths

Porosity of a rock is constant during an undrained test. Therefore, the effective-stress path in an undrained test constitutes effective stresses that the rock can have for a certain porosity. Effective-stress paths have thus found a key role in modern prediction of overpressure in subsurface mudrocks from their porosity (Flemings and Saffer, 2018; Goulty, 2004; Hauser et al., 2014; Heidari et al., 2018).

Casey et al. (2016) conducted undrained triaxial tests on RGoM EI mudrocks pre-consolidated under uniaxial-strain condition to different effective vertical stress levels. We show the effective stress path in two of these tests, one at a low pre-consolidation stress of $\sigma'_{v0} = 0.356$ MPa (dashed lines, Fig. 3a) and one at a high pre-consolidation stress of $\sigma'_{v0} = 63.47$ MPa (dashed lines, Fig. 3b). Each path begins with a uniaxial-strain (K_0) stress state (solid points, Fig. 3) and ends at the critical (shear failure) state (hollow points, Fig. 3). We use the original and the new MCC models to predict the effective-stress paths in these two tests. At both stress levels, the new MCC model predicts the effective stress path (green solid line, Fig. 3a; red solid line, Fig. 3b) more accurately than the original MCC model (blue lines, Fig. 3a, b). This is in part due to the fact that the new model predicts the beginning and the end points of the paths more accurately: the location of the beginning points (solid circles, Fig. 3), representing uniaxial-strain pre-consolidation, is a function of the K_0 ratio and the location of the end points (hollow circles, Fig. 3), representing the critical state, is a function of the $\frac{S_u}{\sigma'_{v0}}$ ratio; these ratios are more

accurately predicted by the new MCC model than the original model at the two stress levels (Fig. 1c, d).

We display the effective stress paths in a normalized-stress plot to illustrate the effect of the mudrock's stress-level-dependent behavior on its effective stress path. The effective stress paths predicted by the original MCC model map into a single, stress-level-independent path (blue line, Fig. 3c) (Muir Wood, 1990). The stress paths predicted by the new MCC model, however, map into different, stress-level-dependent paths; the stress path at low stress levels (green solid line, Fig. 3c) is larger than the original model's path (blue line, Fig. 3c), and, as stress level increases, the stress path approaches the original model's path and becomes smaller than this path at high stress levels (red solid line, Fig. 3c).

(a) (b)

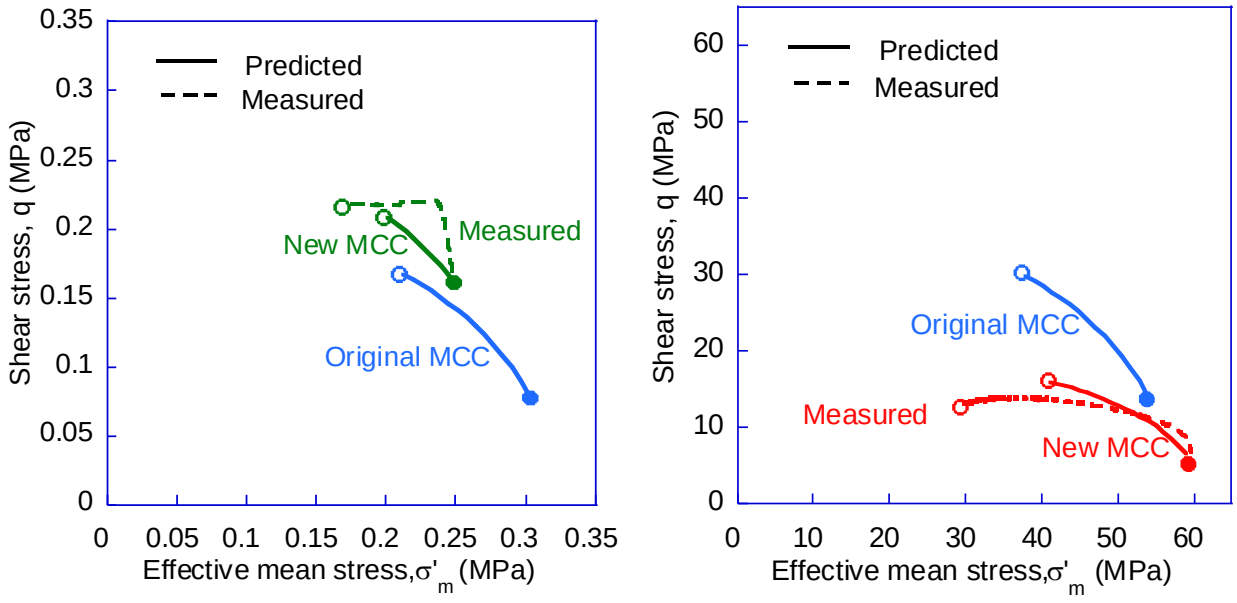

(c)

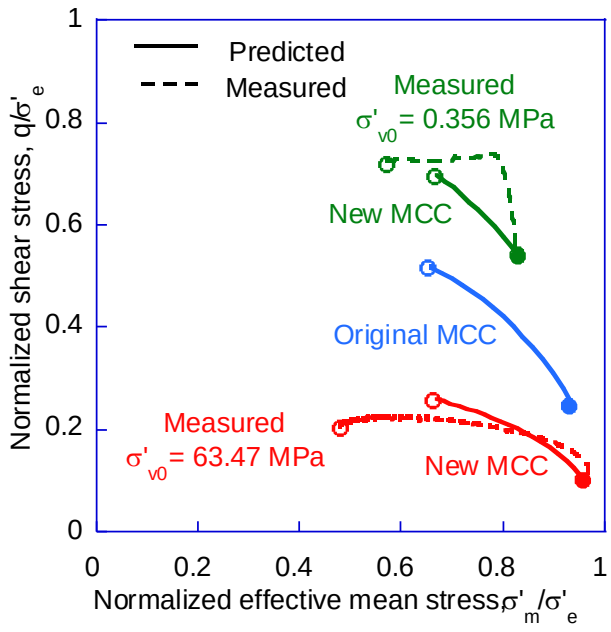

Figure 3: Measured effective stress paths in undrained triaxial tests (dashed line) vs. those predicted by original (blue line) and new (green and red solid lines) MCC model. Measured paths are for RGoM EI mudrocks (Casey et al., 2016). (a) at a low pre-consolidation stress of $\sigma'_{v0} = 0.356$ MPa. (b) at a high pre-consolidation stress of $\sigma'_{v0} = 63.47$ MPa. (c) at both stress levels in a plot with stresses normalized by the equivalent stress (σ'_e), i.e., the horizontal intercept of the paths. The original MCC model produces a single, stress-level-independent path for both stress levels, thereby failing to predict the stress-level-dependent measured paths. In contrast, the new MCC model produces stress-level-dependent paths that successfully predict the measured paths.

2.4 Limitations of new MCC model

Like the original MCC model, the new MCC model describes the intrinsic behavior of mudrocks (Burland, 1990; Fearon and Coop, 2000) and does not include the effects of features such as structure (Liu and Carter, 2002; Suebsuk et al., 2010), cementation (Nguyen et al., 2014), and or anisotropy (Rouainia and Muir Wood, 2000; Whittle and Kavvadas, 1994), which are typically observed in natural mudrocks. The effect of these features could be superimposed on the proposed model.

3 Geological applications

We discuss the impacts of the stress dependency of the friction angle on a range of geological and drilling processes. We study the topography of critical wedges, appropriate drilling mud weights, the Earth's strength profile, and the stability of levees in submarine channels. Analytical models have been developed for these processes assuming a constant friction angle for mudrocks. We revisit and modify these models for a mudrock with a stress-dependent friction angle. The modified models are calibrated for RGoM EI mudrocks and used to quantitatively illustrate the impacts of the stress dependency of the friction angle on the chosen processes. Lastly, we encode the new MCC model and use it in conjunction with a finite-element model to estimate stresses in a salt basin in the Gulf of Mexico.

3.1 Topography of critical wedges

The fold-and-thrust belts and submarine accretionary wedges that lie along compressive plate boundaries are one of the most recognized features of the Earth's crust (Dahlen, 1990; Kearey et al., 2009; Moore and Vrolijk, 1992; Saffer and Tobin, 2011; Stern, 2002). The base of these regions, typically a detachment or décollement fault, commonly dip opposite to the region's surface, resulting in a wedge-shaped cross section (Fig. 4a). Subduction of the plate below critical wedges imposes frictional drag on the wedge along the wedge's base, causing significant lateral deformation in the wedge recorded by elevated porosity loss and abundant imbricate thrust faults and folds.

The critical-taper theory is the most-widely used model to understand the mechanics of critical wedges and quantitatively assess their geometry (Dahlen, 1990; Davis et al., 1983). In this model, it is assumed that the lateral drag imposed by the subducting plate on the wedge brings sediments within the wedge to the Coulomb frictional failure. Based on this assumption,

359 the wedge angle ($\alpha_w + \beta_w$, Fig. 4a) is at a critical, maximum value. Davis et al. (1983) used
360 equilibrium equations and derived equations to estimate the wedge angle for a thin-skinned,
361 critical wedge with rocks of constant friction angle. Dahlen (1990) and Skarbek and Rempel
362 (2017) improved these equations for wedges with spatially varying (heterogeneous) properties.
363 We use these equations and derive the angle for a wedge with stress-dependent friction angle.
364 For a wedge with hydrostatic pore pressure, this angle is

$$\alpha_w + \beta_w = \frac{dH}{dX} = \frac{1 - \sin(\phi_{mb})}{1 + \sin(\phi_{mb})}(\beta_w + \mu_b); \quad (9)$$

365 where ϕ_{mb} is the friction angle of the rocks at the stress level that exists at the base of the
366 wedge. H is the wedge thickness, which varies with distance from the toe of the wedge (X).
367 Parameter μ_b is the sliding friction coefficient on the décollement, which can be expressed as
368 $\mu_b = \tan(\phi_b)$, where ϕ_b is the Coulomb friction angle for sliding on the décollement. In
369 general, in order for slip to occur on the decollement, the décollement must be frictionally
370 weaker than adjacent rocks. If pore pressure in the décollement is the same as that in adjacent
371 rocks, this requires that $\phi_b \leq \phi_{mb}$ (e.g., Davis et al., 1983). Equation 9 is the same as the
372 equation for the angle of a wedge with a constant friction angle φ (see Equation 16 in Dahlen
373 (1990)) if φ is replaced with φ_{mb}.

374 We use Equation 9 to calculate the angle of a thin-skinned submarine (accretionary) wedge
375 composed of RGoM EI mudrocks and under hydrostatic pore pressure. The décollement has a
376 dip of $\beta_w = 2^o$ and a constant sliding friction coefficient of $\mu_b = 0.12$. The bulk density of
377 mudrocks in the wedge is $\rho = 2.4\ gr/cc$, and the density of pore water is $\rho_w = 1.0\ gr/cc$. We
378 first calculate the friction angle φ_{mb}, which varies along the wedge because the stress level at the
379 base of the wedge varies along the wedge due to the wedge thickening: given the hydrostatic
380 pore pressure in the wedge, the effective vertical stress at the base of the wedge is obtained as a

function of the wedge thickness as $\sigma_v' = (\rho - \rho_w)gH$, where g is the gravitational acceleration. Because in a thin-skinned critical wedge, horizontal stress is the maximum stress, σ_v' is the least effective principal stress. The stress-dependent friction angle of mudrocks can be described as a function of different stress measures. Here, because the least principal stress is known, we describe the friction angle as a function of the least principal stress. To determine this function for RGoM EI mudrocks, the friction angle measured at each stress level (Table 2) is cross plotted against the effective least principal stress at that stress level (points, Fig. 4b) and then a function that best fits the data points is chosen, which is a power-law function for RGoM EI mudrocks (line, Fig. 4b). This curve is used with σ_v' to calculate ϕ_{mb}. The resulting friction angle is a function of the wedge thickness (H), turning Equation 9 into a first-order differential equation. We integrate this equation numerically to find the wedge thickness along the wedge ($H(X)$) and then to find the wedge angle ($\frac{dH}{dX}$).

(a)

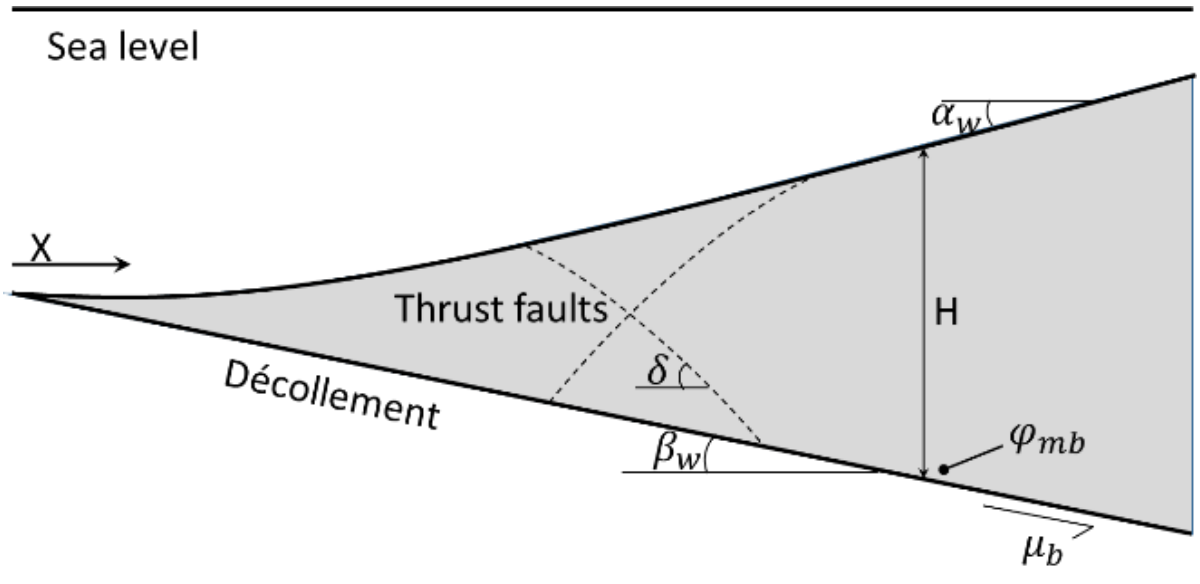

(b) (c)

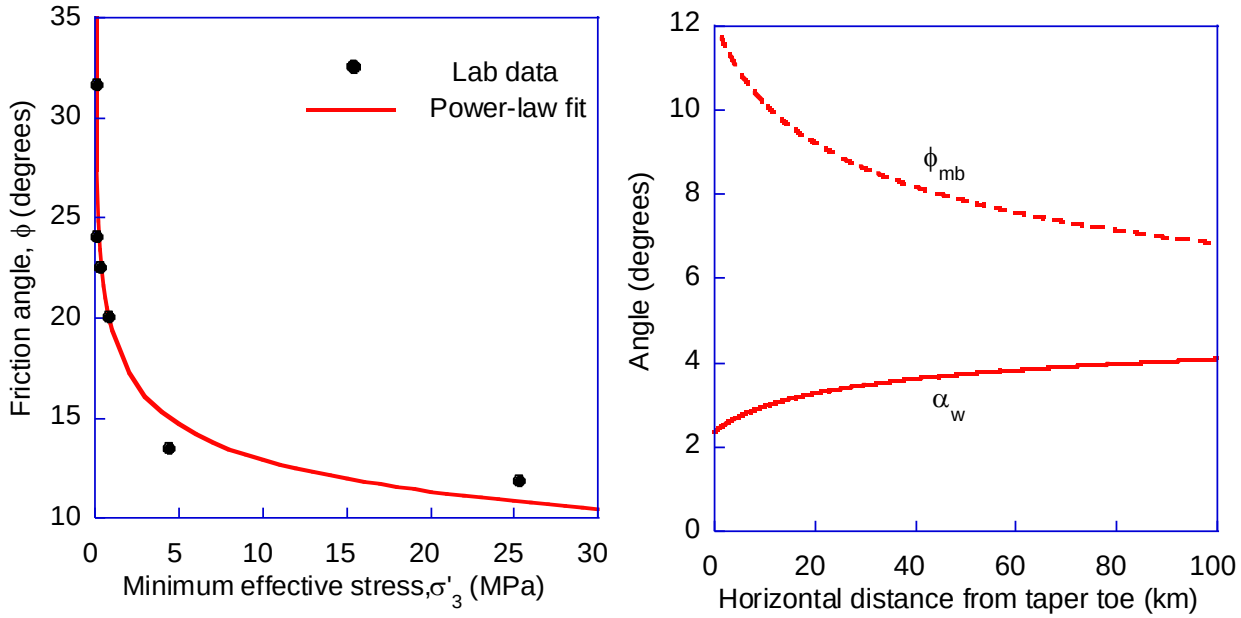

(d)

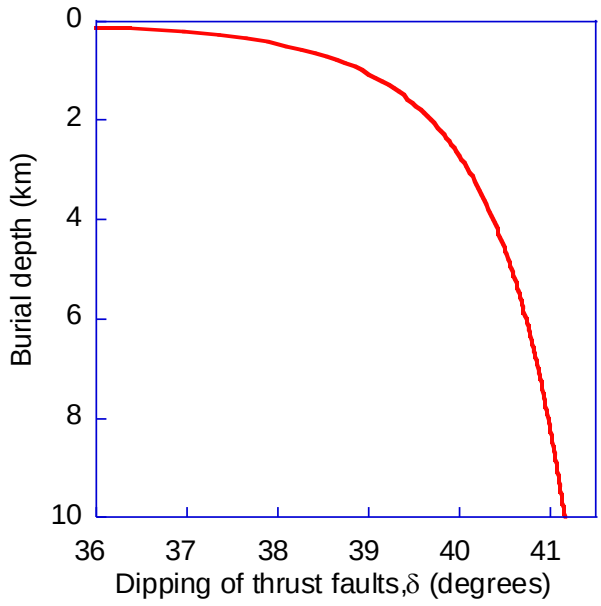

Figure 4: Profiles predicted for topography and thrust faults of an accretionary wedge composed of mudrocks with stress-dependent friction angle. (a) Schematics of profiles. (b) Friction angle of mudrocks within the wedge as a function of minimum effective stress. Lab data are for RGoM EI mudrocks (Casey et al., 2016). (c) Friction angle of mudrocks at the overburden stress at the base of the wedge (ϕ_{mb}) and the slope of the wedge topography (α) along the wedge. (d) Dipping of thrust faults over depth.

408 The stress dependency of the friction angle results in a wedge angle that increases with
409 distance from the toe of the wedge (α_w, Fig. 4c), resulting in a concave topographic surface for
410 the wedge (Fig. 4a). The reason is that as distance from the toe of the wedge increases, the
411 overburden stress at the base of the wedge increases with increase in the wedge thickness, and
412 the friction angle at the base thus decreases (φ_{mb}, Fig. 4c), resulting in higher wedge angle
413 (Equation 9). The dipping of the wedge surface changes at a rapid rate near the toe and a much
414 slower rate far from the toe (Fig. 4a; α_w, Fig. 4c), reflecting rapid change of friction angle at low
415 stresses near the toe and its slow change at high stresses far from the toe (Fig. 4b; φ_{mb}, Fig. 4c).
416 This profile is markedly different from the linear profile that a constant friction angle predicts
417 (constant φ_{mb}, Equation 9).

418 We also investigate how the stress dependency of the friction angle affects the dipping of
419 thrust faults in the wedge. Given that, in a thin-skinned critical wedge, the maximum stress is
420 almost horizontal and the least principal stress is almost vertical, thrust faults have a dip of
421 nearly $\delta = 45^o - \frac{\phi}{2}$, where ϕ is the friction angle of the rocks in the wedge. We calculate the dip
422 of thrust faults over the depth of a wedge with RGoM EI mudrocks by calculating the friction
423 angle over depth. The friction angle at any given depth is calculated by using the effective
424 vertical stress at that depth in the friction angle-least principal stress power-law relationship
425 (line, Fig. 4b). The stress dependency of the friction angle results in a dip angle that increases
426 with depth (δ, Fig. 4d), resulting in a convex profile for thrust faults (Fig. 4a). The increase in
427 the dip angle with depth results from an increase in the overburden stress with depth and the
428 associated decrease in friction angle (Fig. 4b), resulting in increase in the dip angle with depth
429 ($\delta = 45^o - \frac{\phi}{2}$). The dip angle changes at a rapid rate near the surface of the wedge and at a much
430 slower rate deep in the wedge (Figs. 4a, d), reflecting rapid change of friction angle at low

stresses near the surface of the wedge and its slow change at high stresses deep in the wedge (Fig. 4b). This fault profile differs markedly from the planar profile that a constant friction angle predicts.

Our prediction of a concave profile for the wedge surface agrees with the finding of Dahlen et al. (1984), who predicted this profile for critical wedges with rocks that have cohesion in addition to friction angle. This agreement derives from the fact that the Mohr failure envelope of rocks with a stress-dependent friction angle is a curvilinear curve (red solid line, Fig. 2) that can be approximated by a tangent linear envelope with cohesion.

Natural examples of critical wedges with concave surface and convex thrust faults are scarce. One reason could be that the predicted change in the surface angle (α_w, Fig. 4c) along the wedge is not larger than the margin of error for the measurement of this angle (Dahlen et al., 1984). Another reason could be that the surface concavity is canceled out or even reversed by other processes that produce convexity of the wedge surface. Examples of these processes include increase in rock cohesion due to lithification or decrease in overpressure with distance from the toe of the wedge (Zhao et al., 1986) and decrease in porosity with depth (Breen and Orange, 1992).

In contrast to the scarcity of convex thrust faults, there are abundant examples for concave listric normal faults in extensional settings, which can be explained by the stress dependency of the friction angle. In extensional settings, the maximum stress is vertical and the minimum stress is horizontal, thus, faults have a dip angle of $45^o + \phi/2$. In contrast to thrust faults, the decrease of friction angle with depth due to increase in stresses produces a decrease in the dip angle with depth, resulting in a concave profile for faults.

454 3.2 Appropriate drilling mud-weights

455 It is common practice to maintain the pressure of drilling mud in the open (uncased) section
456 of a wellbore to be less than the least principal stress in the surrounding formation (σ_3). This
457 practice limits outflow of drilling mud into formations due to extensive hydraulic fracturing and
458 consequently loss of the drilling mud. The least principal stress in a formation consolidated
459 under purely vertical, uniaxial strain is

$$\sigma_3 = K_0 \cdot \sigma_v' + u \quad (10)$$

460 where σ_v' is the effective vertical stress, and u is pore pressure. It is also common practice to
461 maintain the pressure of the drilling mud to be higher than a minimum pressure ($P_{collapse}$) to
462 prevent excessive breakout of wall rocks (Willson and Fredrich, 2005; Zoback, 2010). If no
463 drainage occurs in wall rocks during drilling of a wellbore (undrained conditions), the collapse
464 pressure $P_{collapse}$ for a vertical wellbore in a uniaxially-consolidated formation is (Kirsch, 1898)

$$P_{collapse} = \sigma_3 - S_u, \quad (11)$$

465 where S_u is the undrained strength. Mud pressures between σ_3 and $P_{collapse}$ are thus appropriate
466 pressures for drilling.

467 To show how the stress dependency of the friction angle of the formation rocks affects
468 appropriate drilling mud pressures, we calculate σ_3 and $P_{collapse}$ along a vertical wellbore in a
469 formation composed of RGoM EI mudrocks and consolidated uniaxially under hydrostatic pore
470 pressure. To calculate σ_3 for a given depth, we calculate the effective vertical stress (σ_v') at that
471 depth by subtracting hydrostatic pore pressure (u_h) from the overburden stress (σ_v) ($\sigma_v' = \sigma_v -$
472 u_h). The calculated σ_v' is then used in the K_0-σ_v' relationship for RGoM EI mudrocks (red solid
473 line, Fig. 1c) to calculate K_0 (red solid line, Fig. 5a). Finally, the calculated K_0 and σ_v' are used in
474 Equation 10 ($\sigma_3 = K_0 \cdot \sigma_v' + u_h$) to calculate σ_3. The calculated σ_3 is shown along the wellbore

in Equivalent Mud Weight, $EMW\ (\text{ppg}) = \frac{\sigma_3\ (\text{MPa})}{Depth\ (\text{km})} * 0.85 \frac{(\text{ppg})}{\left(\frac{\text{MPa}}{\text{km}}\right)}$ (red solid line, Fig. 5b), which is a common way to illustrate this stress in wellbore drilling. To calculate $P_{collapse}$ for a given depth, the calculated σ_v' for that depth is used in $\frac{S_u}{\sigma_{v0}'}$-σ_v' relationship for RGoM EI mudrocks (solid line, Fig. 1d) to calculate $\frac{S_u}{\sigma_{v0}'}$ ratio and hence S_u by multiplying the ratio by σ_v'. Finally, the calculated S_u and σ_3 are used in Equation 11 to calculate $P_{collapse}$, which is shown along the wellbore in Equivalent Mud Weight, $EMW\ (\text{ppg}) = \frac{P_{collapse}\ (\text{MPa})}{Depth\ (\text{km})} * 0.85 \frac{(\text{ppg})}{\left(\frac{\text{MPa}}{\text{km}}\right)}$ (red dashed line, Fig. 5b). We also calculate σ_3 and $P_{collapse}$ along the wellbore (blue lines, Fig. 5b) for the case a constant, average value is chosen for the friction angle of RGoM mudrocks (dashed line, Fig. 1b). The K_0 and $\frac{S_u}{\sigma_{v0}'}$ ratios in this case are constant along the wellbore (blue lines, Fig. 5a). Approximating the stress-dependent friction angle with a constant, average value results in the followings:

1) underestimation of the K_0 ratio and the least principal stress (σ_3) at non-shallow depths. Because a constant friction angle does not capture the decrease of the friction angle with stress (Fig. 1b), the K_0 ratio that it produces underestimates this ratio at high stresses (Fig. 1c) at non-shallow depths (solid lines, Fig. 5a), leading to underestimation of the least principal stress at these depths (Equation 10) (solid lines, Fig. 5b).
2) overestimation of the $\frac{S_u}{\sigma_{v0}'}$ ratio and the difference ($\sigma_3 - P_{collapse}$) at non-shallow depths. Because the constant friction angle does not capture the decrease of the friction angle with stress (Fig. 1b), the $\frac{S_u}{\sigma_{v0}'}$ ratio that it produces overestimates this ratio and thus the undrained strength (S_u) at high stresses (Fig. 1d) at non-shallow depths (dashed lines,

Fig. 5a). Because the difference ($\sigma_3 - P_{collapse}$) equals the undrained strength (S_u) (Equation 11), this leads to overestimation of this difference at these depths (shaded areas, Fig. 5b).

Approximating the friction angle with a constant, average value thus leads to underestimating the magnitudes of appropriate mud weights and overestimating the margin of these mud weights ($\sigma_3 - P_{collapse}$) (shaded areas, Fig. 5b).

(a)

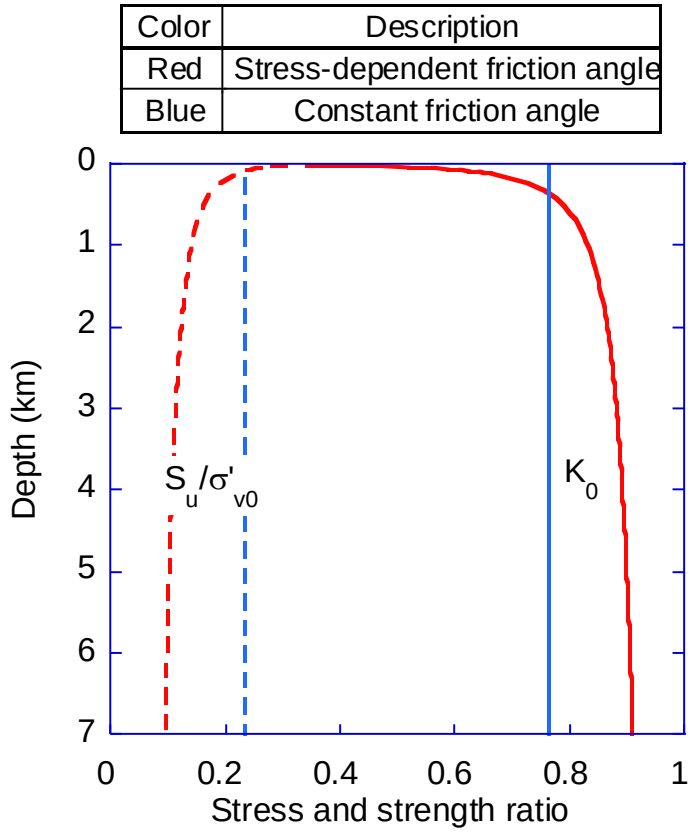

(b)

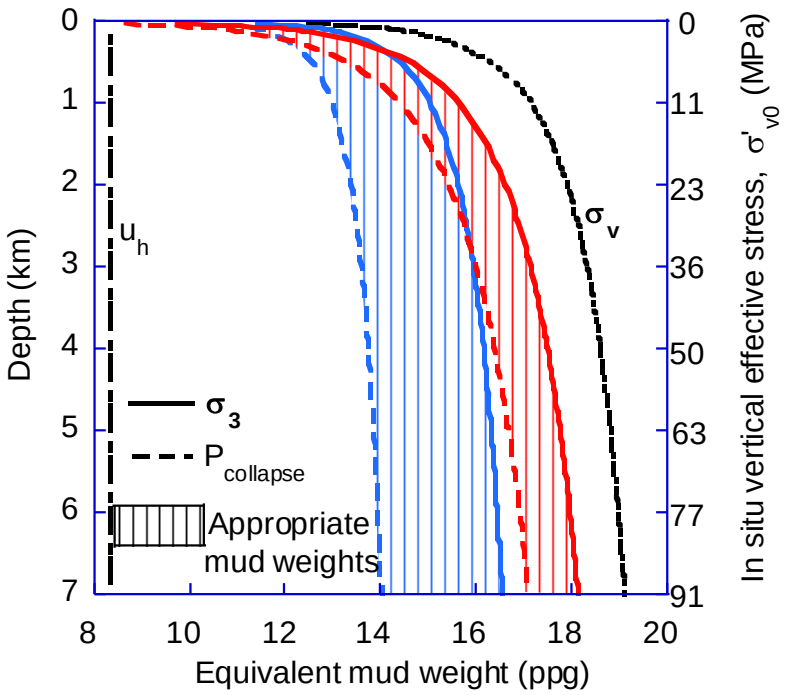

Fig. 5: Stress and strength ratios and appropriate mud weights predicted along a vertical wellbore with and without considering the stress dependency of the friction angle. (a) Stress ratio (K_0) and undrained strength ratio ($\frac{S_u}{\sigma'_{v0}}$) over depth. (b) Minimum stress (σ_3), minimum mud pressure necessary for wellbore stability ($P_{collapse}$), and appropriate mud weights over depth. u_h represents hydrostatic pressure, and σ_v represents lithostatic stress.

3.3 Stability of submarine channel systems

Rotational, deep-seated levee failure is common in submarine channels (Bohn et al., 2012; Jobe et al., 2011; Sawyer et al., 2014; Winker and Shipp, 2002). These failures cause large volumes of sediments to fail from the channel levees into the channel, significantly affecting the form and function of the channel-levee system.

Gibson and Morgenstern (1962) and later Hunter and Schuster (1968) analyzed the circular failure of submarine levees. Consider a mass in a levee delineated by a circular cut through the levee (Fig. 6a). The moment that the weight of the mass produces around the center of the circular cut (**W**·l, Fig. 6a) drives the down-slope rotational failure of the mass. This failure is

resisted by the moment that the shear strength of rocks along the circular cut produces ($\int_0^{2\alpha} S_u\, R^2 d\theta$, Fig. 6a). The stability of a levee is controlled by a mass that has the lowest ratio of resisting to driving moments. This lowest ratio is called the safety factor of the levee. A levee is stable if its safety factor is greater than one, unstable if its safety factor is smaller than one, and at the verge of failure if its safety factor is one.

Gibson and Morgenstern (1962) and Hunter and Schuster (1968) calculated the safety factor for levees with a constant strength ratio ($\frac{S_u}{\sigma'_{v0}}$) and hydrostatic pore pressure. We revisit their analysis for levees with overpressure and stress-dependent strength ratio. In a levee with angle β and height h (Fig. 6a) and assuming that the rocks of the levee have consolidated uniaxially and have a uniform overpressure ratio ($\lambda^* = \frac{u-u_h}{\sigma_v-u_h}$), we obtain the ratio of driving to resisting moments for a mass with angles α and γ (Fig. 6a) as

$$\frac{3\,(1-\lambda^*)\int_0^{2\alpha} \frac{S_u}{\sigma'_{v0}}\, z\, d\theta}{h\, G(\alpha,\gamma,\beta)}, \qquad for\ \ 0<\gamma<\beta \quad and \quad 0<\alpha<\frac{\pi}{2} \tag{12}$$

where $G(\alpha,\gamma,\beta) = sin^2\alpha\, sin^2\gamma\ [1 - 2\, cot^2\beta + 3\,(cot\gamma\, cot\beta + cot\gamma\, cot\alpha - cot\alpha\, cot\beta)]$, and z is depth from the updip surface of the levee (Fig. 6a). We calculate the safety factor by finding the lowest value of this ratio among different angles α and γ.

To show the impact of the stress dependency of the friction angle on the analysis of levees, we use our model to analyze deep-seated rotational failures in the levees of submarine channels in Ursa Basin, Gulf of Mexico (Sawyer et al., 2014). In these levees, $\beta = 10^o$, $h = 275\, m$, and $\rho = 2\ gr/cc$. We use the friction angles of RGoM EI mudrocks for these levees assuming that mudrocks in the two regions of the Gulf of Mexico (Ursa Basin and Eugene Island) have similar mechanical properties. Because failure has occurred in these levees, the safety factor is one. We

use this to back-calculate the overpressure ratio (λ^*) in these levees at the time of failure. For levees with a constant friction angle, the maximum stable levee angle can be described as a function of the reduced undrained strength ratio ($\frac{S_u}{\sigma'_{v0}}(1-\lambda^*)$) (Fig. 6b). If the friction angle of mudrocks in the Ursa Basin levees is approximated with a constant, average value ($\varphi = 21^o$; Fig. 1b), the undrained strength ratio is $\frac{S_u}{\sigma'_{v0}} = 0.23$ (dashed line, Fig. 1d); for this strength ratio and the angle of the Ursa Basin levees ($\beta = 10^o$), the overpressure ratio is obtained as $\lambda^* = 0.62$ (circle, Fig. 6b). In contrast, if the stress dependency of the friction angle is taken into account (solid line, Fig. 1b), a lower overpressure ratio of $\lambda^* = 0.54$ is obtained. Assuming a constant friction angle leads to overestimation of the overpressure ratio because the constant friction angle does not capture the decrease of the friction angle with stress (Fig. 1b), so the strength ratio that it produces overestimates this ratio at high stresses (Fig. 1d) in non-shallow rocks of the levee (dashed lines, Fig. 5a). Because of overestimating the strength of the levee rocks, the constant friction angle requires higher overpressures for the levee to fail.

(a)

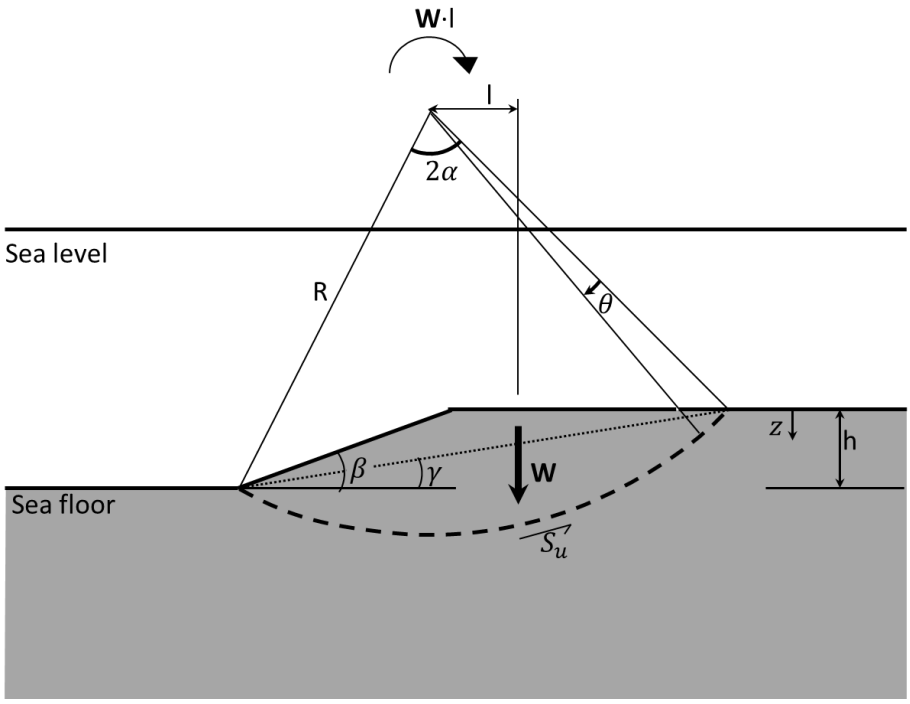

(b)

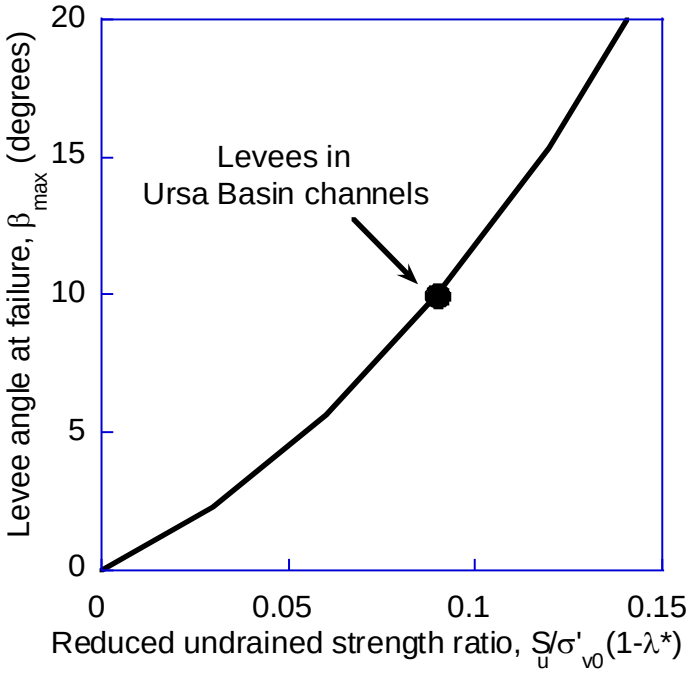

Fig. 6: Stability of a submarine levee against deep-seated rotational failure. (a) Schematics of slope and circular failure surface. Weight of failing mass (W) drives down-slope rotation of the mass, and shear strength of rocks (S_u) along the failure surface resists this rotation. (b) Levee angle at failure as a function of reduced undrained strength ratio.

564

565 3.4 Strength profile of Earth's crust

566 The stress difference in rocks cannot exceed the rock strength. This notion has been used to
567 set limits on the in situ stress difference in the Earth's crust. The rock strength, according to the
568 Coulomb criterion, can be expressed as:

$$\sigma_1 - \sigma_3 = \frac{2\sin(\phi)}{1+\sin(\phi)}\sigma_1'. \quad (13)$$

569 where σ_1 is the total maximum principal stress, and σ_1' is the effective maximum principal stress.

570 A constant value for the friction angle is typically used to estimate the rock strength (e.g.,
571 Suppe, 2014; Zoback et al., 1993). To show the impact of the stress dependency of the friction
572 angle on the estimation of the rock strength-depth profiles, we use Equation 13 to predict the
573 rock strength along a wellbore in Brazos or Corsair region of offshore Texas, Gulf of Mexico
574 (Xiao et al., 1991) taking into account the stress dependency of the friction angle. Estimates of
575 the rock strength are available along the well (hollow circles, Fig. 7c), allowing us to evaluate
576 the predicted rock strengths. These estimates are based on leak-off tests carried out at several
577 depths along the well (Xiao et al., 1991). These tests provide an estimate of the least principal
578 stress (σ_3). The estimated σ_3 are subtracted from the overburden stress (σ_1) to calculate stress
579 difference ($\sigma_1 - \sigma_3$). Because the well lies in a region of active normal faults, the calculated
580 stress differences are inferred to equal the rock strength. We use the friction angles of RGoM EI
581 mudrocks in our prediction of the rock strength assuming that mudrocks in the two regions of the
582 Gulf of Mexico (Brazos and Eugene Island) have similar mechanical properties. We calculate σ_1'
583 in Equation 13 by subtracting pore pressure from the overburden stress ($\sigma_1' = \sigma_v - u$), where
584 pore pressure, u, is estimated from sonic logs along the wellbore. The estimated pore pressure is
585 almost hydrostatic along the wellbore above a well-defined depth and increases almost parallel to

586 the lithostatic gradient below this depth (solid line; Fig. 7b). As a result, stress σ_1' increases
587 above the overpressure-onset depth and is approximately constant below this depth (dashed line,
588 Fig. 7b). To calculate the friction angle ϕ in Equation 13, because σ_1' is known along the well,
589 we describe the friction of mudrocks (Table 2) as a function of σ_1'. This function is determined
590 by cross plotting friction angles measured in the experimental tests against the effective
591 maximum stress (Table 2; points, Fig. 7a) and fitting an appropriate function to the data points,
592 which is a power-law function for RGoM EI mudrocks (solid line, Fig. 7a). This function is used
593 with the calculated σ_1' along the wellbore (dashed line, Fig. 7b) to calculate the friction angle
594 along the wellbore.

595 If a typical, low-stress, constant value is used for the friction angle (e.g., $\phi = 24^o$; green
596 dashed line, Fig. 7a), the predicted strengths are a constant factor of σ_1' (Equation 13), therefore,
597 they increase linearly above the overpressure-onset depth and remain constant below this depth
598 (green dashed line, Fig. 7c). The predicted strengths disagree with the strengths estimated from
599 leak-off tests (hollow circles, Fig. 7c). In contrast, if the stress dependency of the friction angle is
600 taken into account (red solid line, Fig. 7a), the predicted strengths are variable factors of σ_1'
601 (Equation 13), therefore, they increase nonlinearly above the overpressure-onset depth (red solid
602 line, Fig. 7c). Taking into account the stress dependency of the friction angle substantially
603 improves prediction of the rock strengths. The small discrepancy between the predicted and the
604 estimated rock strengths (red solid line vs. points, Fig. 7c) could be from possible difference
605 between the mechanical properties, in particular the friction angle, of intact mudrocks at the
606 wellbore site (Brazos) and RGoM EI mudrocks used in our analysis, which could be due to
607 possible difference in the lithology of these two mudrocks or due to the intact versus
608 resedimented states of the two mudrocks.

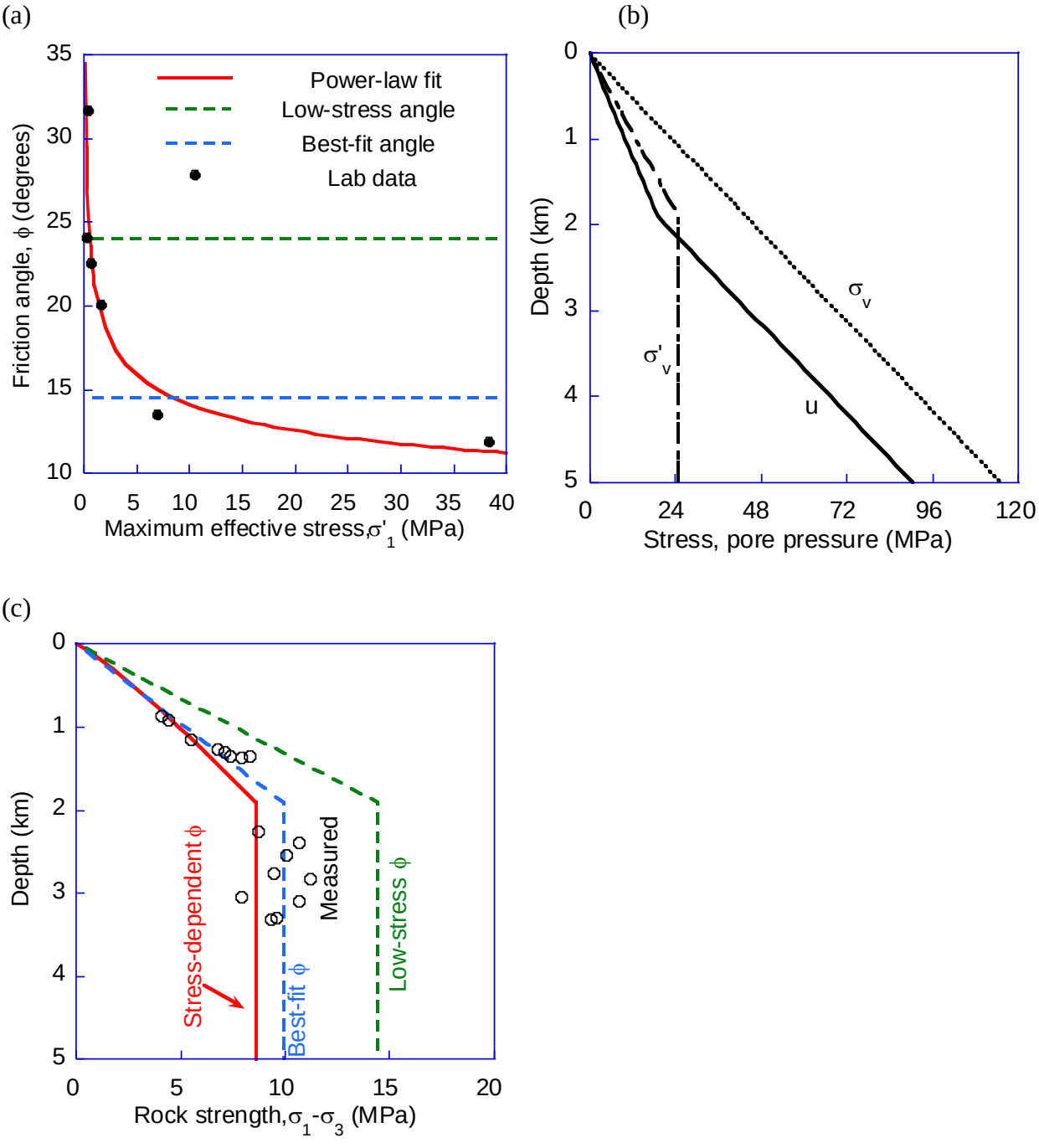

Fig. 7: Earth strength profiles predicted along a wellbore in offshore Texas, Gulf of Mexico (Suppe, 2014; Xiao et al., 1991) with and without considering the stress dependency of the friction angle. (a) Friction angle as a function of maximum effective stress. Lab data are for RGoM EI mudrocks (Casey et al., 2016). (b) Pore pressure, lithostatic stress, and effective vertical stress over depth (modified after Suppe (2014)). Pore pressure is estimated from sonic velocity log. (c) Predicted earth strength profiles (lines) vs. strengths estimated from leak-off tests (hollow circles) (modified after Suppe (2014)).

We also find the constant friction angle that provides the best fit (blue dashed line, Fig. 7c) to the estimated rock strengths (hollow circles, Fig. 7c). This friction angle ($\phi = 14^o$; blue dashed line, Fig. 7a) is markedly lower than typical values used for the friction angle of mudrocks (e.g., $\phi = 24^o$). Previous studies, which assume a constant friction angle, attribute this anomalously low friction angle to possibly very weak clay-rich smear gouges in normal faults in the well region (Brown et al., 2003; Numelin et al., 2007; Suppe, 2014). Our analysis, in contrast, suggests that the low friction angle indicated by the well data could result from a significant decrease of the friction angle with stress (red solid line, Fig. 7a).

3.5 Stress field in a salt basin

We estimate stresses around a submarine salt body below the Sigsbee Escarpment in Mad Dog Field, deepwater Gulf of Mexico (Fig. 8a). The strain and stress states of the rocks can differ significantly from those at purely vertical, uniaxial strain because of the salt body and the significant topography at the Sigsbee Escarpment (Fig. 8a). The Escarpment updip rocks tend to move laterally toward the Escarpment downdip, resulting extension in updip rocks and compression in downdip rocks. As a result, lateral strain below the Escarpment is far different from zero and stresses are thus far different from those under purely vertical, uniaxial strain. In contrast with other rocks, salt rock relaxes the differential (shear) stress over geologic time. This can impose significant changes to the magnitude and orientation of strain and stress in rocks surrounding salt, resulting in stresses that are far different from those under uniaxial strain condition (Fredrich et al., 2003; Heidari et al., 2017; Nikolinakou et al., 2014). The magnitude

644 and extent of the stress changes that the salt and the basin topography cause depend on the 3D
645 mechanical behavior of the rocks surrounding the salt body.

646 We use the original and the new MCC models for rocks. This allows us to assess the impact
647 of the stress-level-dependent behavior of the rocks on stresses. The constitutive equations of the
648 MCC models are integrated numerically using the backward Eulerian method and then encoded
649 as a UMAT subroutine. This subroutine is linked to the finite-element model of the salt basin
650 that we build in code Abaqus to estimate stresses (DassaultSystems, 2013; Nikolinakou et al.,
651 2013).

652 The finite-element model is a 2D plane-strain model. Horizontal displacement is fixed at the
653 side boundaries and vertical displacement is fixed at the bottom boundary of the model (Fig. 8a).
654 Salt is modeled as a nearly incompressible (compressibility coefficient, $\kappa_{salt} = 0.01$) poro-
655 elastic material with small shear stiffness (shear modulus, G=0.01 MPa). The density of salt is
656 22.00 gr/cm^3. The mechanical parameters of RGoM EI mudrocks are used for rocks in our model
657 assuming that rocks in the Mad Dog field have similar properties as those in Eugene Island. The
658 density of rocks is 22.53 gr/cm^3. Pore pressure is assumed to be hydrostatic everywhere in the
659 model (drained analysis). The model begins with almost zero initial stresses everywhere and then
660 the weight of salt and sediments is applied gradually over time. Stresses are obtained after the
661 entire weight is applied.

662 The ratio of minimum to maximum effective stress predicted by the original MCC model
663 (Fig. 8b) significantly differs from the value of this ratio at uniaxial strain condition (K_0=0.76;
664 Fig. 1c) particularly in subsalt rocks. The significant change in the seabed topography at Sigsbee
665 Escarpment leads to a decreases in the stress ratio in the updip rocks, including rocks below salt
666 and to the left of the salt body. This decrease is reversed in rocks to the left of the salt body by a

667 higher increase in the stress ratio that the lateral push from salt causes, resulting in stress ratios in
668 this area higher than the K_0 ratio (Fig. 8b).

669 The new MCC model predicts significantly different stresses. For example, it predicts that
670 the stress ratio is higher (Fig. 8c) than predicted by the original MCC model in non-shallow
671 rocks (Fig. 8b). This could be attributed to the fact that the friction angle at high stresses in non-
672 shallow rocks is lower in the new MCC model (solid line, Fig. 1b) than the average value used in
673 the original model (dashed line, Fig. 1b).

674
675 (a)

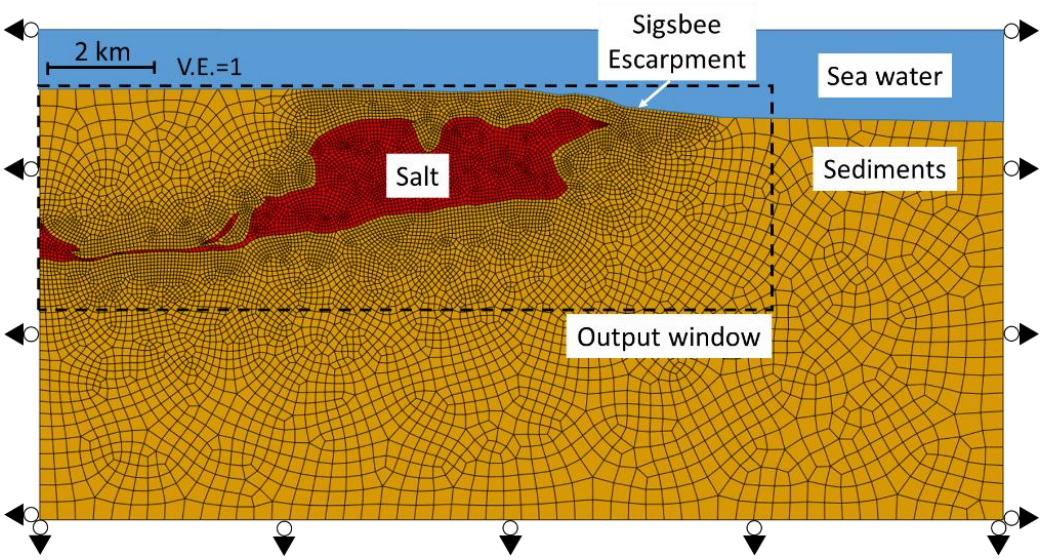

676
677 (b)

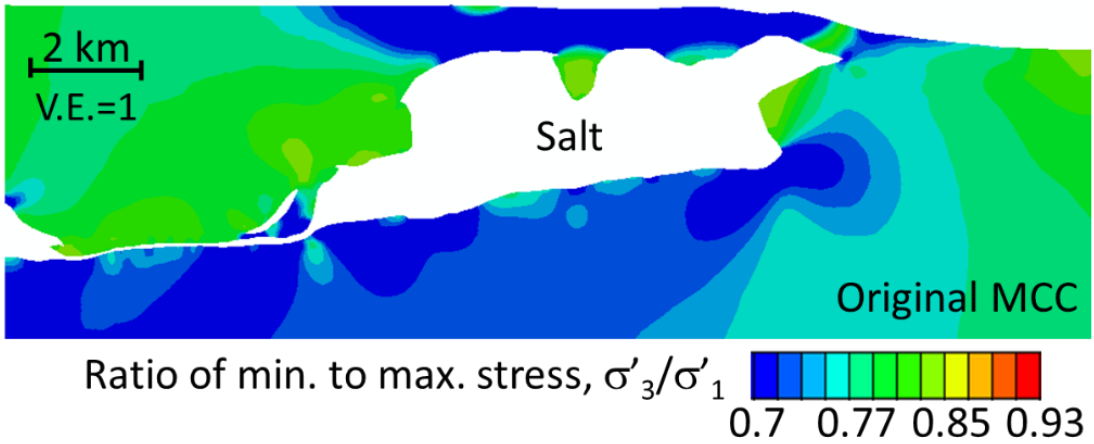

678
679 (c)

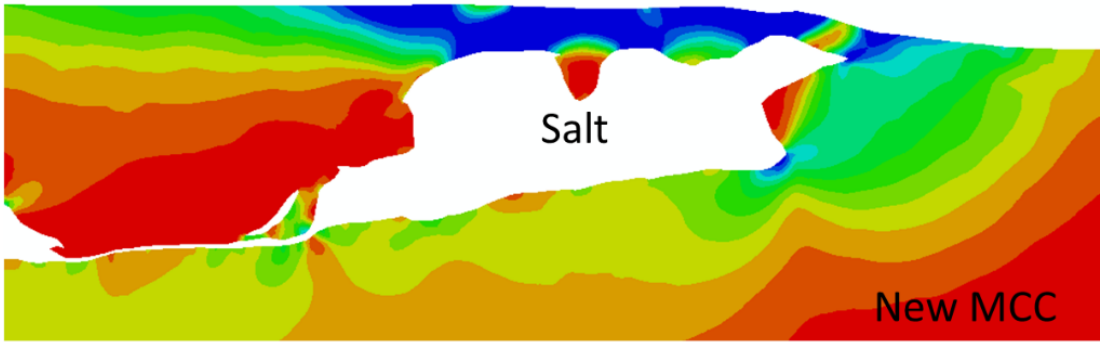

Figure 8: Plane-strain finite-element model of a salt basin in Mad Dog Field, deepwater Gulf of Mexico. Geometry of salt body and seabed topography are based on seismic data provided by BP & Partners. (a) Finite-element mesh and boundary conditions. (b) Ratio of minimum to maximum effective stress predicted by original MCC model. (c) Ratio of minimum to maximum effective stress predicted by new MCC model.

4 Conclusions

We modify the MCC model to incorporate the decrease of the friction angle and the slope of the compression curve with stress over large stress ranges encountered in geological settings (up to 100 MPa). With only one additional parameter, the new model successfully predicts variation of the stress and undrained-strength ratios with stress. We encode the new MCC model to use it in conjunction with a finite-element model of a salt basin. The new model predicts significantly different stresses around salt than the original MCC model.

We also demonstrate the implications of the stress dependency of the friction angle for drilling wellbores and geological processes such as the topography of critical wedges, stability of submarine channel levees, and the strength profile of the Earth's crust. We revisit and modify analytical models developed for these processes and show that the decrease of the friction angle with stress has significant consequences. It causes 1) a concave topography for critical wedges and convex profile for thrust faults in these wedges; 2) higher magnitudes and a narrower margin of appropriate mud weights for drilling a wellbore; and 3) failure of submarine channel levees at a lower angle.

Our study could improve estimation of stresses, pore pressure, appropriate mud weights for drilling wellbores, and quantitative analysis of geological processes that depend on the friction angle.

Acknowledgements

This study was funded by the UT GeoFluids and AGL consortia, and Jackson School of Geosciences at The University of Texas at Austin. AGL is supported by (http://www.beg.utexas.edu/agl/sponsors), and UT GeoFluids is supported by Anadarko, BHP Billiton, BP, Chevron, Conoco-Phillips, ExxonMobil, Hess, Pemex, Repsol, Shell, and Statoil. Datasets for this research are included in Casey et al. (2016).

Appendix A. Thermomechanics of the new MCC model

A constitutive model must be able to simulate experimental observations successfully. This, nonetheless, is not sufficient; a constitutive model must also satisfy thermodynamics principles. The second principle of thermomechanics states that, during elastic deformation, the material conserves the mechanical work done by stresses; as a result, no energy is stored or dissipated at the end of a loading-unloading cycle. The volumetric elastic equation in the original MCC model (Eqn. 2) results in an energy-conserving elastic model if it is used along with a constant shear modulus; Zytynski et al. (1978) showed that the variable shear modulus obtained from the bulk modulus and a constant Poisson's ratio does not yield an energy-conserving model. Houlsby (1985) and Borja et al. (1997) proposed variable shear moduli that conserved energy. It can be easily shown that the new volumetric elastic equation that we propose (Eqn. 8) conserves energy if used with a constant shear modulus. Variable shear moduli that conserve energy could also be

derived for the new volumetric equation following the approach taken by Houlsby (1985) and Borja et al. (1997).

The second principle of thermomechanics also requires that, during plastic deformation, part of the mechanical work done by stresses dissipate; in other words, the dissipation, defined as the total mechanical work less the energy stored in the material, is positive. In the original MCC model, the increment of dissipation ($d\Phi$) that occurs during an increment of plastic deformation ($d\boldsymbol{\varepsilon^p}$) is (Collins and Kelly, 2002)

$$d\Phi = \sigma'_{m_{cr}}[\left(d\varepsilon_v^p\right)^2 + \left(M \cdot d\varepsilon_\gamma^p\right)^2]^{\frac{1}{2}}$$

$$> 0 \qquad (A-1)$$

where $\sigma'_{m_{cr}} = \frac{\sigma'_{m_0}}{2}$, and $d\varepsilon_v^p$ and $d\varepsilon_\gamma^p$ are the volumetric and deviatoric parts of $d\boldsymbol{\varepsilon^p}$, respectively. The dissipation increment in the new MCC model is given by the same equation but with a parameter M that is not constant and a function of $\sigma'_{m_{cr}}$ (Eqn. 6). Thus, like the original MCC model, the new MCC model meets the thermomechanics requirement of a positive dissipation during plastic deformation.

References

Abdulhadi, N. O., Germaine, J. T., and Whittle, A. J., 2012, Stress-dependent behavior of saturated clay: Canadian Geotechnical Journal, v. 49, no. 8, p. 907-916.

Alberty, M. W., and McLean, M. R., 2004, A Physical Model for Stress Cages, SPE Annual Technical Conference and Exhibition: Houston, Texas, Society of Petroleum Engineers, p. 8.

Atkinson, J. H., and Bransby, P., 1977, The mechanics of soils, an introduction to critical state soil mechanics, 0042-3114.

Bishop, A., Webb, D., and Lewin, P., 1965, Undisturbed samples of London Clay from the Ashford Common shaft: strength–effective stress relationships: Geotechnique, v. 15, no. 1, p. 1-31.

Bohn, C. W., IV, Flemings, P. B., and Slingerland, R. L., 2012, Accommodation Change During Bypass Across a Late-Stage Fan in the Shallow Auger Basin

Application of the Principles of Seismic Geomorphology to Continental Slope and Base-of-Slope Systems: Case Studies from SeaFloor and Near-Sea Floor Analogues, *in* Prather, B. E., Deptuck, M. E.,

Mohrig, D., Hoorn, B. V., and Wynn, R. B., eds., Volume 99, SEPM Society for Sedimentary Geology, p. 0.
Borja, R. I., Tamagnini, C., and Amorosi, A., 1997, Coupling plasticity and energy-conserving elasticity models for clays: Journal of geotechnical and geoenvironmental engineering, v. 123, no. 10, p. 948-957.
Breen, N. A., and Orange, D. L., 1992, The effects of fluid escape on accretionary wedges 1. Variable porosity and wedge convexity: Journal of Geophysical Research: Solid Earth, v. 97, no. B6, p. 9265-9275.
Brooker, E. W., and Ireland, H. O., 1965, Earth pressures at rest related to stress history: Canadian geotechnical journal, v. 2, no. 1, p. 1-15.
Brown, K. M., Kopf, A., Underwood, M. B., and Weinberger, J. L., 2003, Compositional and fluid pressure controls on the state of stress on the Nankai subduction thrust: A weak plate boundary: Earth and Planetary Science Letters, v. 214, no. 3, p. 589-603.
Burland, J., 1990, On the compressibility and shear strength of natural clays: Géotechnique, v. 40, no. 3, p. 329-378.
Butterfield, R., 1979, A natural compression law for soils: Géotechnique, v. 29, no. 4, p. 469-480.
Casey, B., Germaine, J. T., Flemings, P. B., and Fahy, B. P., 2016, In situ stress state and strength in mudrocks: Journal of Geophysical Research: Solid Earth, v. 121, no. 8, p. 5611-5623.
Casey, B., Reece, J., and Germaine, J., 2019, One-dimensional normal compression laws for resedimented mudrocks: Marine and Petroleum Geology.
Collins, I., and Kelly, P., 2002, A thermomechanical analysis of a family of soil models: Geotechnique, v. 52, no. 7, p. 507-518.
Cook, A. E., and Sawyer, D. E., 2015, The mud-sand crossover on marine seismic data: Geophysics, v. 80, no. 6, p. A109-A114.
Dahlen, F., 1990, Critical taper model of fold-and-thrust belts and accretionary wedges: Annual Review of Earth and Planetary Sciences, v. 18, no. 1, p. 55-99.
Dahlen, F., Suppe, J., and Davis, D., 1984, Mechanics of fold-and-thrust belts and accretionary wedges: Cohesive Coulomb theory: Journal of Geophysical Research: Solid Earth, v. 89, no. B12, p. 10087-10101.
DassaultSystems, 2013, Commercial finite element code Abaqus 6.13-2.
Davis, D., Suppe, J., and Dahlen, F. A., 1983, Mechanics of fold-and-thrust belts and accretionary wedges: Journal of Geophysical Research: Solid Earth, v. 88, no. B2, p. 1153-1172.
Fearon, R., and Coop, M., 2000, Reconstitution: what makes an appropriate reference material?: Géotechnique, v. 50, no. 4, p. 471-477.
Flemings, P. B., and Saffer, D. M., 2018, Pressure and Stress Prediction in the Nankai Accretionary Prism: A Critical State Soil Mechanics Porosity-Based Approach: Journal of Geophysical Research: Solid Earth, p. n/a-n/a.
Flemings, P. B., Stump, B. B., Finkbeiner, T., and Zoback, M., 2002, Flow focusing in overpressured sandstones: Theory, observations, and applications: American Journal of Science, v. 302, no. 10, p. 827-855.
Fredrich, J. T., Coblentz, D., Fossum, A. F., and Thorne, B. J., 2003, Stress perturbations adjacent to salt bodies in the deepwater Gulf of Mexico, Society of Petroleum Engineers Annual Technical Conference and Exhibition: Denver, Colorado, 2003. Society of Petroleum Engineers.
Gao, B., Flemings, P. B., Nikolinakou, M. A., Saffer, D. M., and Heidari, M., 2018, Mechanics of Fold-and-Thrust Belts Based on Geomechanical Modeling: Journal of Geophysical Research: Solid Earth, v. 0, no. 0.
Gibson, R., and Morgenstern, N., 1962, A note on the stability of cuttings in normally consolidated clays: Geotechnique, v. 12, no. 3, p. 212-216.

798 Goulty, N., 2004, Mechanical compaction behaviour of natural clays and implications for pore pressure
799 estimation: Petroleum Geoscience, v. 10, no. 1, p. 73-79.
800 Hart, B. S., Flemings, P. B., and Deshpande, A., 1995, Porosity and pressure: Role of compaction
801 disequilibrium in the development of geopressures in a Gulf Coast Pleistocene basin: Geology, v.
802 23, no. 1, p. 45-48.
803 Hashiguchi, K., Isotropic Hardening Theory for Granular Media, *in* Proceedings Proceedings of the Japan
804 Society of Civil Engineers1974, Volume 1974, Japan Society of Civil Engineers, p. 45-60.
805 -, 1995, On the linear relations of v–ln p and ln v–ln p for isotropic consolidation of soils: International
806 journal for numerical and analytical methods in geomechanics, v. 19, no. 5, p. 367-376.
807 Hauser, M. R., Couzens-Schultz, B. A., and Chan, A. W., 2014, Estimating the influence of stress state on
808 compaction behavior: Geophysics, v. 79, no. 6, p. D389-D398.
809 Heidari, M., Nikolinakou, M. A., and Flemings, P. B., 2018, Coupling geomechanical modeling with
810 seismic pressure prediction: GEOPHYSICS, v. 83, no. 5, p. B253-B267.
811 Heidari, M., Nikolinakou, M. A., Flemings, P. B., and Hudec, M. R., 2017, A simplified stress analysis of
812 rising salt domes: Basin Research, v. 29, no. 3, p. 363-376.
813 Holtz, R. D., and Kovacs, W. D., 1981, An introduction to geotechnical engineering, v. Monograph.
814 Houlsby, G., 1985, The use of a variable shear modulus in elastic-plastic models for clays: Computers and
815 Geotechnics, v. 1, no. 1, p. 3-13.
816 Hubbert, M., and Rubey, W. W., 1959, Role of fluid pressure in mechanics of overthrust faulting:
817 I.Mechanics of fluid-filled porous solids and its application to overthrust faulting: Geological
818 Society of America Bulletin, v. 70, no. 2, p. 115-166.
819 Hunter, J. H., and Schuster, R., 1968, Stability of simple cuttings in normally consolidated clays:
820 Geotechnique, v. 18, no. 3, p. 372-378.
821 Ikari, M. J., Saffer, D. M., and Marone, C., 2007, Effect of hydration state on the frictional properties of
822 montmorillonite-based fault gouge: Journal of Geophysical Research: Solid Earth, v. 112, no. B6.
823 Jaky, J., 1948, Pressure in silos: Proc. 2nd ICSM, 1948.
824 Jobe, Z. R., Lowe, D. R., and Uchytil, S. J., 2011, Two fundamentally different types of submarine canyons
825 along the continental margin of Equatorial Guinea: Marine and Petroleum Geology, v. 28, no. 3,
826 p. 843-860.
827 Jones, C. A., 2010, Engineering properties of resedimented Ugnu clay from the Alaskan north slope:
828 Massachusetts Institute of Technology.
829 Kearey, P., Klepeis, K. A., and Vine, F. J., 2009, Global tectonics, John Wiley & Sons.
830 Kirsch, C., 1898, Die theorie der elastizitat und die bedurfnisse der festigkeitslehre: Zeitschrift des
831 Vereines Deutscher Ingenieure, v. 42, p. 797-807.
832 Liu, M., and Carter, J., 2002, A structured Cam Clay model: Canadian Geotechnical Journal, v. 39, no. 6,
833 p. 1313-1332.
834 Mayne, P. W., and Kulhawy, F. H., 1982, Ko- OCR Relationships in Soil: Journal of the Soil Mechanics and
835 Foundations Division, v. 108, no. 6, p. 851-872.
836 McDowell, G., and Hau, K., 2003, A simple non-associated three surface kinematic hardening model:
837 Géotechnique, v. 53, no. 4, p. 433-437.
838 Mesri, G., and Hayat, T., 1993, The coefficient of earth pressure at rest: Canadian Geotechnical Journal,
839 v. 30, no. 4, p. 647-666.
840 Mesri, G., and Olson, R. E., 1971, Consolidation characteristics of montmorillonite: Geotechnique, v. 21,
841 no. 4, p. 341-352.
842 Moore, D. E., and Lockner, D. A., 2007, Friction of the smectite clay montmorillonite: The seismogenic
843 zone of subduction thrust faults, p. 317-345.
844 Moore, J. C., and Vrolijk, P., 1992, Fluids in accretionary prisms: Reviews of Geophysics, v. 30, no. 2, p.
845 113-135.

846 Muir Wood, D., 1990, Soil Behaviour and Critical State Soil Mechanics, Cambridge, U.K., Cambridge
847 University Press, 462 p.:
848 Nguyen, L. D., Fatahi, B., and Khabbaz, H., 2014, A constitutive model for cemented clays capturing
849 cementation degradation: International Journal of Plasticity, v. 56, p. 1-18.
850 Nikolinakou, M. A., Flemings, P. B., and Hudec, M. R., 2014, Modeling stress evolution around a rising
851 salt diapir: Marine and Petroleum Geology, v. 51, p. 230-238.
852 Nikolinakou, M. A., Merrell, M. P., Luo, G., B., F. P., and Hudec, M. R., 2013, Geomechanical modeling of
853 the Mad Dog salt, Gulf of Mexico, 47th US Rock Mechanics Symposium: San Francisco, CA, 23-26
854 June, 2013.
855 Numelin, T., Marone, C., and Kirby, E., 2007, Frictional properties of natural fault gouge from a low-angle
856 normal fault, Panamint Valley, California: Tectonics, v. 26, no. 2.
857 Pestana, J. M., and Whittle, A., 1995, Compression model for cohesionless soils: Géotechnique, v. 45, no.
858 4, p. 611-631.
859 Roscoe, K. H., and Burland, J. B., 1968, On the generalized stress-strain behaviour of "wet" clay, *in*
860 Heyman, J., ed., Engineering Plasticity: Cambridge, England, Cambridge University Press, p. 535-
861 609.
862 Rouainia, M., and Muir Wood, D., 2000, A kinematic hardening constitutive model for natural clays with
863 loss of structure: Géotechnique, v. 50, no. 2, p. 153-164.
864 Saffer, D. M., and Marone, C., 2003, Comparison of smectite-and illite-rich gouge frictional properties:
865 application to the updip limit of the seismogenic zone along subduction megathrusts: Earth and
866 Planetary Science Letters, v. 215, no. 1-2, p. 219-235.
867 Saffer, D. M., and Tobin, H. J., 2011, Hydrogeology and Mechanics of Subduction Zone Forearcs: Fluid
868 Flow and Pore Pressure: Annual Review of Earth and Planetary Sciences, v. 39, no. 1, p. 157-186.
869 Sawyer, D. E., Flemings, P. B., and Nikolinakou, M., 2014, Continuous deep-seated slope failure recycles
870 sediments and limits levee height in submarine channels: Geology, v. 42, no. 1, p. 15-18.
871 Skarbek, R. M., and Rempel, A. W., 2017, Heterogeneous Coulomb wedges: Influence of fluid pressure,
872 porosity, and application to the Hikurangi subduction margin, New Zealand: Journal of
873 Geophysical Research: Solid Earth, v. 122, no. 3, p. 1585-1613.
874 Stern, R. J., 2002, Subduction zones: Reviews of geophysics, v. 40, no. 4, p. 3-1-3-38.
875 Stigall, J., and Dugan, B., 2010, Overpressure and earthquake initiated slope failure in the Ursa region,
876 northern Gulf of Mexico: Journal of Geophysical Research: Solid Earth, v. 115, no. B4.
877 Suebsuk, J., Horpibulsuk, S., and Liu, M. D., 2010, Modified Structured Cam Clay: A generalised critical
878 state model for destructured, naturally structured and artificially structured clays: Computers
879 and Geotechnics, v. 37, no. 7-8, p. 956-968.
880 Suppe, J., 2007, Absolute fault and crustal strength from wedge tapers: Geology, v. 35, no. 12, p. 1127-
881 1130.
882 -, 2014, Fluid overpressures and strength of the sedimentary upper crust: Journal of Structural Geology,
883 v. 69, p. 481-492.
884 Velde, B., 1996, Compaction trends of clay-rich deep sea sediments: Marine Geology, v. 133, no. 3, p.
885 193-201.
886 Whittle, A. J., and Kavvadas, M. J., 1994, Formulation of MIT-E3 constitutive model for overconsolidated
887 clays: Journal of Geotechnical Engineering, v. 120, no. 1, p. 173-198.
888 Willson, S. M., and Fredrich, J. T., 2005, Geomechanics considerations for through- and near-salt well
889 design, SPE Annual Technical Conference and Exhibition: Dallas, Texas, Society of Petroleum
890 Engineers, p. 1-17.
891 Winker, C. D., and Shipp, R. C., 2002, Sequence Stratigraphic Framework for Prediction of Shallow Water
892 Flow in the Greater Mars-Ursa Area, Mississippi Canyon Area, Gulf of Mexico Continental Slope

Sequence Stratigraphic Models for Exploration and Production: Evolving Methodology, Emerging Models and Application Histories, *in* Armentrout, J. M., and Rosen, N. C., eds., Volume 22, SEPM Society for Sedimentary Geology, p. 0.

Xiao, H. B., Dahlen, F., and Suppe, J., 1991, Mechanics of extensional wedges: Journal of Geophysical Research: Solid Earth, v. 96, no. B6, p. 10301-10318.

Yassir, N. A., 1989, Mud volcanoes and the behaviour of overpressured clays and silts: University of London.

Zhao, W. L., Davis, D., Dahlen, F., and Suppe, J., 1986, Origin of convex accretionary wedges: Evidence from Barbados: Journal of Geophysical Research: Solid Earth, v. 91, no. B10, p. 10246-10258.

Zoback, M. D., 2010, Reservoir Geomechanics, Cambridge University Press.

Zoback, M. D., Apel, R., Baumgärtner, J., Brudy, M., Emmermann, R., Engeser, B., Fuchs, K., Kessels, W., Rischmüller, H., and Rummel, F., 1993, Upper-crustal strength inferred from stress measurements to 6 km depth in the KTB borehole: Nature, v. 365, no. 6447, p. 633.

Zytynski, M., Randolph, M., Nova, R., and Wroth, C., 1978, On modelling the unloading-reloading behaviour of soils: International Journal for Numerical and Analytical Methods in Geomechanics, v. 2, no. 1, p. 87-93.